Enhancement of giant magnetoelectric effect in Ni-doped CaBaCo₄O₇

M. Gen [1,2,*] A. Miyake [2] H. Yagiuchi,[1] Y. Watanabe,[1] A. Ikeda [2] Y. H. Matsuda [2] M. Tokunaga [2,3]
T. Arima,[1,3,†] and Y. Tokunaga[1]

[1]*Department of Advanced Materials Science, University of Tokyo, Kashiwa 277-8561, Japan*
[2]*Institute for Solid State Physics, University of Tokyo, Kashiwa 277-8581, Japan*
[3]*RIKEN Center for Emergent Matter Science (CEMS), Wako 351-0198, Japan*

The polar magnet CaBaCo₄O₇ is known to exhibit the largest magnetic-field-driven electric polarization change (ΔP) associated with an antiferromagnetic- (AFM-) ferrimagnetic (FIM) transition in a narrow temperature range between 62 and 69 K. In this paper, we investigate the effect of Ni doping on its multiferroic properties by means of magnetization, electric polarization, dielectric constant, and magnetostriction measurements on single crystals of CaBaCo₃.₉Ni₀.₁O₇ up to 50 T. In the doped material, two kinds of AFM phases appear below 78 K, accompanying negative ΔP. Upon the application of a magnetic field along any crystallographic axis, giant positive ΔP of up to 11 to 12 mC/m² is observed along with an AFM-FIM transition in the whole temperature range below 78 K. The giant magnetoelectric effect inherent in CaBaCo₄O₇ can be further enhanced just by a small amount of chemical substitution in terms of: (i) increasing the magnitude of ΔP and (ii) expanding the temperature range in which giant ΔP appears.

I. INTRODUCTION

Since the discovery of the electric polarization switching associated with a magnetic phase transition in TbMnO₃ [1], the search for spin-driven ferroelectricity and the relating magnetoelectric (ME) phenomena has been a central issue in condensed-matter physics [2]. Spin cycloid with a net vector spin chirality, $\mathbf{S}_i \times \mathbf{S}_j$, was first considered as a major source of spin-driven ferroelectricity [3–6]. Subsequently, a variety of magnetic states, including a collinear spin structure, were found to potentially produce electric polarization, which can be explained by the d-p hybridization [7,8] or the exchange striction mechanisms [9–11]. For exploring nontrivial ME responses, frustrated spin systems are recognized as a promising playground because an external magnetic field can induce phase transitions among nearly degenerate magnetic states [12].

The swedenborgite CaBaCo₄O₇ (CBCO), which belongs to a polar orthorhombic space-group $Pbn2_1$, is known as a multiferroic material with magnetic frustration [13–24]. The crystal structure is composed of an alternate stacking of kagome and triangular layers of CoO₄ tetrahedra as shown in Fig. 1(a). The buckling distortion in the kagome layers results in four inequivalent Co sites and induces a charge ordering of Co2/Co3 sites with Co²⁺ and Co1/Co4 sites with Co³⁺($3d^6/3d^7\underline{L}$) [13,14]. The high-temperature magnetization measurement evidences a large negative Weiss temperature $\Theta_{CW} = -890$ K and the development of an antiferromagnetic (AFM) short-range order below ∼360 K [15].

On cooling, the system undergoes a transition to an AFM state at $T^* \approx 69$ K and finally enters a ferrimagnetic (FIM) ground state at $T_C \approx 62$ K [16–19], where the Co2/Co3 spins form ferromagnetic zigzag chains with the easy axis along the b axis and the Co1/Co4 spins point roughly antiparallel to them [14]. The magnetic transition from the AFM to the FIM phase takes place also when applying a magnetic field along the b axis in an intermediate-temperature range of $T_C < T < T^*$ [Fig. 1(b)] [17,18]. Remarkably, the AFM-FIM transition accompanies a giant electric polarization change of $\Delta P \approx 8$ mC/m² along the c axis, which is the largest value reported to date [17–19]. Due to the nonswitchable character of the electric polarization direction, CBCO is classified as pyroelectric [17]. According to the previous neutron diffraction and thermal expansion measurements, the emergence of the FIM state is accompanied by an abrupt decrease in the lattice constant c [14,17,18], suggesting that the giant ME effect is attributed to the exchange striction [21,22].

From the viewpoint of magnetism, the effect of partial chemical substitution on CBCO was systematically studied by many researchers [25–34]. One approach is the divalent Sr²⁺ substitution for the nonmagnetic Ca²⁺/Ba²⁺, revealing that a few percent of Sr doping significantly suppresses the FIM ordering whereas maintaining the orthorhombic crystal structure [26–28]. This signals that the ferrimagnetism in undoped CBCO is quite sensitive to the local structural distortion. Another approach is the substitution for the magnetic Co, and it has been pointed out that the selective substitution of sites with the target valence is possible by a small amount of doping up to ∼20 % [29–34]. In the case of the nonmagnetic Al³⁺/Ga³⁺ substitution for Co³⁺, the magnetic order is statistically destroyed at the benefit of magnetic frustration even though the Co2/Co3 ferromagnetic chains remain

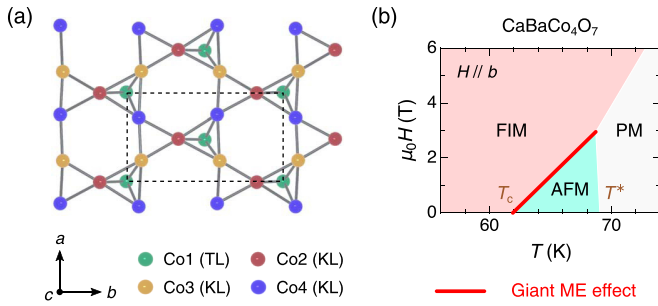*masaki.gen@riken.jp
†arima@k.u-tokyo.ac.jp

FIG. 1. (a) Schematic of the c-axis projection of the Co network in the swedenborgite lattice of $CaBaCo_4O_7$. The dashed rectangle represents the unit cell, which contains four inequivalent Co sites: Co1 on the triangular lattice (TL) and Co2, Co3, and Co4 on the distorted kagome lattice (KL). Note that the kagome and triangular layers are alternately stacked along the c axis, and the neighboring kagome layers alter their orientations by $180°$. For simplicity, only half of the lattice ($0 \leqslant z \leqslant 1/2$) is shown. Co atoms in the kagome layers can be preferentially substituted by a small amount of Ni [34]. (b) Magnetic phase diagram of undoped $CaBaCo_4O_7$ for $H \parallel b$, illustrated based on Refs. [16–20]. A giant ΔP is observed at the AFM-FIM phase boundary between 62 and 69 K (red line).
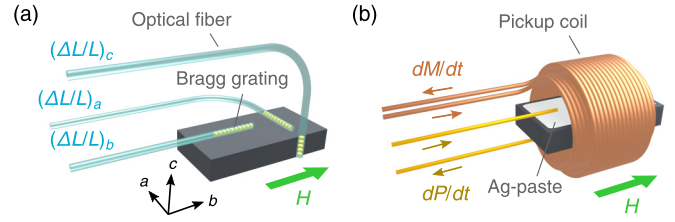

FIG. 2. Experimental configurations for (a) simultaneous three-axial magnetostriction/thermal expansion measurements in static magnetic fields and (b) simultaneous magnetization and electric polarization measurements in pulsed high magnetic fields. Both figures are illustrated for $H \parallel b$.

untouched. As a consequence, the FIM ground state is gradually suppressed and the spin- (or cluster-) glass-like behavior develops with increasing the doping level [29,30]. Of particular interest is the divalent ion substitution for Co^{2+}, which directly affects the Co2/Co3 ferromagnetic chains. In contrast to Al^{3+}/Ga^{3+} doping, only a few percent of nonmagnetic Zn^{2+} doping abruptly weakens the ferrimagnetism and instead leads to an AFM ground state where the fragmented Co2/Co3 ferromagnetic chains would be distributed and couple antiferromagnetically with each other [29,32]. Similarly, magnetic Ni^{2+} doping has been also found to enhance the antiferromagnetism and brings a collinear AFM ground state [34].

Bearing in mind that giant ΔP is linked to the AFM-FIM transition in CBCO, one can expect that Zn^{2+} or Ni^{2+} doping, which brings AFM ground states as mentioned above, is a promising approach to control/enhance the ME effect. Such a study, however, has been so far limited to the polycrystalline samples of Ni-doped CBCO [33,34]. In this paper, we report a single-crystal investigation of the ME effect in $CaBaCo_{3.9}Ni_{0.1}O_7$ (CBCNO) by means of magnetization, electric polarization, dielectric constant, and magnetostriction measurements up to 50 T. In zero field, CBCNO undergoes successive magnetic transitions at $T_{N1} = 78$ and $T_{N2} = 62$ K both of which are found to accompany a negative change in ΔP along the c axis. Strikingly, giant positive ΔP of up to 11 to 12 mC/m² is observed along with the field-induced AFM-FIM transition in the whole temperature range below T_{N1}. In other words, Ni doping on CBCO dramatically increases the magnitude of ΔP itself as well as expands the temperature range exhibiting giant ΔP. We also present the anisotropic nature of magnetostructural transitions and the accompanied ME responses of CBCNO in detail.

II. EXPERIMENTAL METHODS

Single crystals of $CaBaCo_{4-x}Ni_xO_7$ ($x = 0.1$) were grown by the floating zone method under air as in Ref. [19].

Here, NiO was additionally mixed with the starting ingredients in stoichiometric proportions. At the end of growth, the crystal rod was quenched down to room temperature. Single-phase $CaBaCo_{4-x}Ni_xO_7$ was obtained near the top of the crystal rod, which was confirmed by the powder x-ray diffraction pattern on crushed single crystals. Scanning electron microscopy-energy dispersive x-ray analysis revealed the chemical composition of $x = 0.096$, in agreement with the target value ($x = 0.1$) within the measurement accuracy.

The magnetization M up to 7 T was measured using a commercial magnetometer (magnetic property measurement system, Quantum Design). The electric polarization change ΔP, dielectric constant ε', and magnetostriction/thermal expansion $\Delta L/L$ up to 9 T were measured using a commercial cryostat equipped with a superconducting magnet (physical property measurement system, Quantum Design). ΔP along the c axis was obtained by integrating the pyroelectric current measured by using an electrometer (6517A, Keithley). ε' along the c axis was measured at 10 kHz by using an LCR meter (E4980A, Agilent). $\Delta L/L$ was measured by the fiber-Bragg-grating (FBG) technique using an optical sensing instrument (Hyperion si155, LUNA). Here, the distortions along the three principal axes, $(\Delta L/L)_a$, $(\Delta L/L)_b$, and $(\Delta L/L)_c$, were simultaneously measured by gluing three optical fibers to one crystal sample using epoxy Stycast1266 as illustrated in Fig. 2(a).

M, ΔP, and $\Delta L/L$ up to ~ 50 T were measured using a nondestructive pulsed magnet (~ 11 ms duration for M and ΔP, and ~ 36 ms duration for $\Delta L/L$) installed at the International MegaGauss Science Laboratory of the Institute for Solid State Physics, University of Tokyo, Japan. M was measured by the conventional induction method using a coaxial pickup coil. ΔP along the c axis was obtained by integrating the pyroelectric current [35] after subtracting the 120-K data as the background. Here, M and ΔP were simultaneously measured with the setup illustrated in Fig. 2(b), making it possible to extract unambiguous information on how ΔP develops as the magnetic state changes. The longitudinal $\Delta L/L$ was measured by the FBG technique using the optical filter method [36].

In this paper, we applied a magnetic field in three orthogonal axes. Here, it should be noted that as-grown single crystals of $CaBaCo_{4-x}Ni_xO_7$ contain micrometer-sized trigonally twinned domains with the common c axis due to a hexagonal-to-orthorhombic structural transition at much above room temperature [19,22] (a polarizing microscope

image of domains is shown in Fig. S1 in the Supplemental Material [37]). Therefore, one has to take care of the contributions of three kinds of domains when applying a magnetic field along the b or a axis of one domain as will be discussed in Sec. III D. In the following, the field direction is simply written as "for $H \parallel b$" or "for $H \parallel a$." We prepared three pieces of rectangular parallelpiped crystals obtained from the same crystal rod and used samples No. 1 ($a \times b \times c = 2 \times 4 \times 1$ mm^3) for $H \parallel b$, No. 2 ($4 \times 2 \times 1$ mm^3) for $H \parallel a$, and No. 3 ($2 \times 1 \times 2$ mm^3) for $H \parallel c$ so as to easily perform the simultaneous measurements as mentioned above.

III. RESULTS AND DISCUSSIONS

A. Temperature dependence of ME and dilatometric responses in zero field

Figure 3 shows the temperature dependence of (a) M measured at 1 T for each field direction (M_a, M_b, and M_c), (b) ΔP measured at zero field and 9 T for $H \parallel b$, (c) ε' measured at zero field, and (d) $\Delta L/L$ measured at zero field for CBCNO. At (nearly) zero field, two anomalies indicative of magnetic transitions are clearly observed at $T_{N1} = 78$ and $T_{N2} = 62$ K in all the physical quantities. These observations are almost in accordance with the previous reports on the polycrystalline samples [33,34]. No hysteretic behavior can be seen at T_{N1} whereas a hysteresis is observed around T_{N2} in the M-T curves [Fig. 3(a)], indicating that the transitions at T_{N1} and T_{N2} are of second and first orders, respectively. Note that M_a and M_b exhibit another kink around 35 K, below which the ZFC data largely deviate from the FC data [Fig. 3(a)]. These features would be attributed to the formation of short-range cluster glass introduced by magnetic frustration and randomness as universally observed in various kinds of doped CBCO [25–32]. No corresponding anomalies are observed in other physical quantities, and we will no more discuss these anomalies.

The appearance of an intermediate-temperature AFM (IM-AFM) phase between T_{N1} and T_{N2} in CBCNO is also found in undoped CBCO [Fig. 1(b)]. However, CBCNO exhibits an electric polarization change of $\Delta P = P(T_{N2}) - P(T_{N1}) \approx -2$ mC/m^2 [Fig. 3(b)], in contrast to the undoped case with almost no change in ΔP [19]. This difference in the ME response suggests that the magnetic structure of the IM-AFM phase in CBCNO is different from that in CBCO, which is proposed to be a noncollinear AFM state with a magnetic unit cell doubled along the a axis [19]. Another important effect of Ni doping is the ground state switching from the FIM to the AFM state where a collinear spin configuration is proposed by powder neutron diffraction [33,34]. The AFM character is reflected in the significant suppression of the magnetic moment for $H \perp c$; on cooling from the paramagnetic state, M jumps by ~ 0.3 μ_B/f.u. at T_C and further increases toward low temperatures at 0.01 T for CBCO [19], whereas M gradually increases in the whole temperature range below T_{N1} and eventually reaches only less than 0.1 μ_B/f.u. at 1 T for CBCNO. Here, the ratios M_a/M_c and M_b/M_c at low temperatures in CBCNO are much smaller than those in CBCO [16], indicating that the easy-plane magnetic anisotropy is weakened by Ni doping.
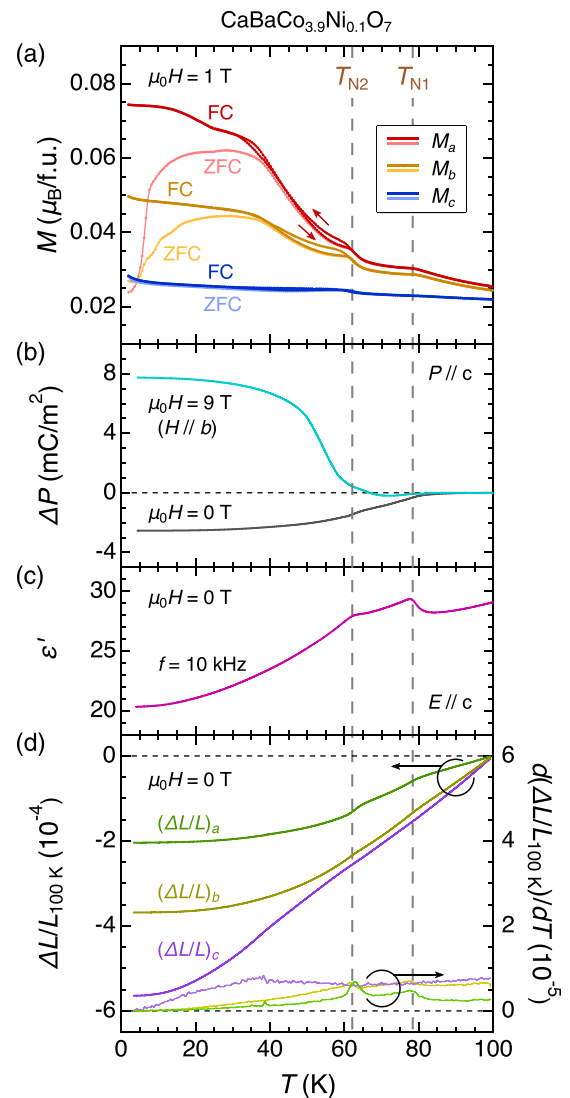

FIG. 3. Temperature dependence of (a) magnetization M measured at 1 T for $H \parallel a$ (sample No. 2), b (No. 1), and c (No. 3) upon warming after zero-field cooling (ZFC), upon field cooling (FC), and the following warming, (b) electric polarization change ΔP along the c axis measured at zero field and 9 T for $H \parallel b$ (No. 1), (c) dielectric constant ε' along the c axis measured at 10 kHz at zero field (No. 2), and (d) thermal expansion $\Delta L/L$ and its temperature derivative along the three principal axes measured at zero field (No. 2). The data in (b)–(d) were obtained upon warming after ZFC.

The ground-state switching also modifies the dilatometric responses. The previous neutron-diffraction experiment on CBCO has revealed increases in the lattice constants a and b upon entering the FIM state [17]. For CBCNO, in contrast, $(\Delta L/L)_a$ and $(\Delta L/L)_b$ monotonically decrease on cooling in the whole temperature range, accompanied by a tiny kink at T_{N1} and T_{N2} [Fig. 3(d)]. Although there remains an ambiguity about the actual changes in the lattice constants a and b due to the presence of trigonally twinned domains, it is reasonable to conclude that both a and b continue to decrease upon entering the AFM state. Moreover, $(\Delta L/L)_c$ does not exhibit any clear anomalies either at T_{N1} or at T_{N2} in CBCNO unlike the case of CBCO in which an abrupt lattice shrinkage takes place
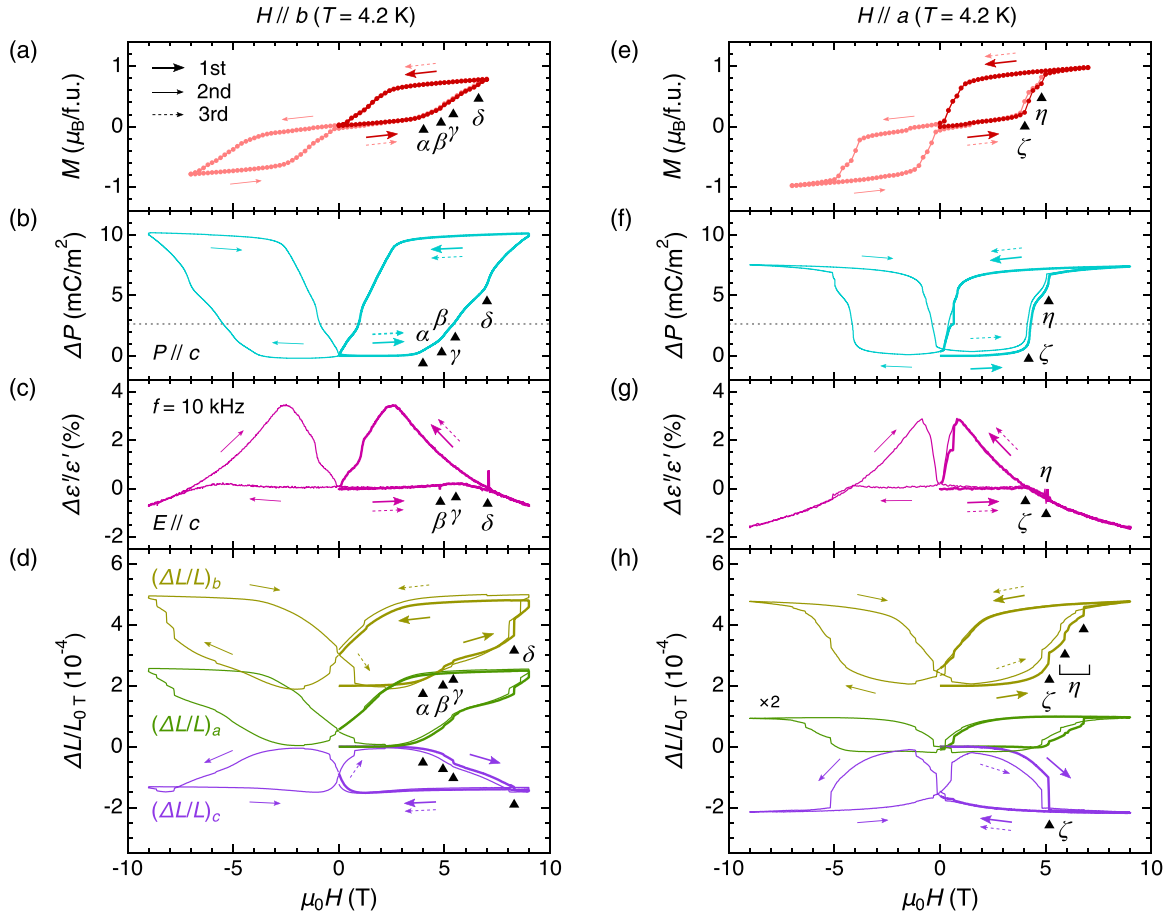
FIG. 4. Magnetic-field dependence of [(a) and (e)] M, [(b) and (f)] ΔP along the c axis, [(c) and (g)] ε' along the c axis, and [(d) and (h)] $\Delta L/L$ along the three principal axes measured at 4.2 K in static magnetic fields for $H \parallel b$ (sample No. 1) [(a)–(d)] and $H \parallel a$ (No. 2) [(e)–(h)]. The dotted lines in (b) and (f) indicate the baseline of electric polarization at 100 K in zero field. ε' was measured at 10 kHz. The data of $(\Delta L/L)_b$ are vertically offset by 2×10^{-4} for clarity. Arrows denote the order of field scans as shown in the inset of (a) where the first scan is $0\,\text{T} \rightarrow 9\,\text{T} \rightarrow 0\,\text{T}$, the second is $0\,\text{T} \rightarrow -9\,\text{T} \rightarrow 0\,\text{T}$, and the third is $0\,\text{T} \rightarrow 9\,\text{T} \rightarrow 0\,\text{T}$. Each measurement was performed after ZFC. The data taken in the first field scan are displayed by thick lines. Triangles with greek letters indicate points where an anomaly is detected in the field-increasing process of the first field scan. Here, the same letters are used for anomalies which are assigned to the identical magnetic-state change. All of these notations are omitted for $(\Delta L/L)_a$, which is qualitatively similar with $(\Delta L/L)_b$.

along the c axis upon entering the FIM state [18]. These observations evidence that the crystal lattice in the AFM state of CBCNO is elongated along the c axis compared to that in the FIM state of CBCO.

These differences highlight how the exchange striction mechanism works in the FIM state of CBCO. In magnetic materials with a strong magnetoelastic coupling, the strain is typically related to the local spin correlator $\langle \mathbf{S}_i \cdot \mathbf{S}_j \rangle$, i.e., the relative angle between the nearest-neighbor spins [38–40]. Since each kagome layer of the Co network is connected via Co1 sites in CBCO, the strain along the c axis should originate from changes in the spin correlators between Co1 and the other Co sites. In this perspective, the crucial difference between the proposed magnetic structure in the FIM state of CBCO [14] and that in the AFM state of CBCNO [34] is in the relative angle between Co1 and Co4 spins, which are almost parallel to each other in the former whereas antiparallel to each other in the latter. Thus, it can be conjectured that the driving force of the magnetostructural transition at T_C in CBCO is the stabilization of ferromagnetic spin alignments

between Co1 and Co4 spins at the cost of the elastic energy, which results in the appearance of ferrimagnetism and the pronounced ME effect.

B. Phase transitions in static magnetic fields up to 9 T

Figure 4 shows the magnetic-field dependence of M, ΔP, ε', and $\Delta L/L$ measured at 4.2 K for $H \parallel b$ [(a)–(d)] and $H \parallel a$ [(e)–(h)]. Here, the sample was cooled down in zero field before measurements with successive field scans of (i) $0\,\text{T} \rightarrow 9\,\text{T} \rightarrow 0\,\text{T}$, (ii) $0\,\text{T} \rightarrow -9\,\text{T} \rightarrow 0\,\text{T}$, and (iii) $0\,\text{T} \rightarrow 9\,\text{T} \rightarrow 0\,\text{T}$. In both configurations, M linearly increases up to $\sim$4 T in the field-increasing process, followed by a sequence of steps indicative of metamagnetic transitions. The M-H loops show a butterfly shape instead of a rectangle shape as observed in CBCO [16], reflecting the ground state switching from the FIM to the AFM state in zero field. Such metamagnetic transitions are not observed for $H \parallel c$ below 9 T (not shown), which is compatible with the existence of the easy-plane magnetic anisotropy.

Importantly, an anisotropy also manifests in the character of the metamagnetic transitions for $H \parallel b$ and $H \parallel a$. When applying a magnetic-field $H \parallel b$, M gradually deviates from the linear field dependence from $\mu_0 H_\alpha \approx 4.0$ T, followed by multistage tiny steps at $\mu_0 H_\beta \approx 4.8$ T, $\mu_0 H_\gamma \approx 5.4$ T, and $\mu_0 H_\delta \approx 6.6$ T [Fig. 4(a)]. These magnetic transitions are accompanied by dielectric anomalies and a clear increase in ΔP, which amounts to ~ 10 mC/m² at 9 T [Figs. 4(b) and 4(c)]. A comparable electric polarization change of $\Delta P \approx 8$ mC/m² can also be induced by sweeping temperature at 9 T [Fig. 3(b)]. The observed ΔP-T curve at 9 T is similar with that for CBCO in zero field [18,19], suggesting the emergence of a field-induced FIM state in CBCNO. Although it is elusive how each spin is oriented with respect to the magnetic field in this field-induced FIM state, we infer that the Co2/Co3 spins are ferromagnetically aligned and the Co1/Co4 spins are antiferromagnetically coupled to them as in the zero-field FIM state of CBCO. In the following, we assume such a state in CBCNO as the FIM state. Notably, the magnitude of the magnetic field-driven ΔP on the AFM-FIM transition in CBCNO is enhanced compared to that in CBCO because there is an additional contribution of the negative ΔP in the initial AFM state as mentioned in Sec. III A. In contrast to the case of $H \parallel b$, the metamagnetic transitions for $H \parallel a$ are rather sharp. The M-H and ΔP-H curves exhibit a jump at $\mu_0 H_\zeta \approx 4.0$ T and a subsequent small jump at $\mu_0 H_\eta \approx 4.8$ T in the field-increasing process for the first field scan [Figs. 4(e) and 4(f)]. Note that these critical fields are a bit higher than those for the second and third field scans possibly due to the pinning effect of magnetic domains. ε' also exhibits a moderate slope change at H_ζ and a spikelike anomaly at H_η [Fig. 4(g)] as in the case of $H \parallel b$ [Fig. 4(c)]. The metamagnetic transitions terminate just above H_η, and ΔP saturates at ~ 7.5 mC/m², which is smaller than that observed for $H \parallel b$.

The multistep AFM-FIM transitions in CBCNO are further supported by the magnetostrictive behaviors, exhibiting multistep elongation along the a and b axes and contraction along the c axis for both field directions with increasing a magnetic field above 4 T [Figs. 4(d) and 4(h)]. Note that the number and/or the positions of anomalies observed in the $\Delta L/L$-H curve are not completely reproducible. This would be owing to the mechanical stress caused by the glue covering the sample surface. From the observed $\Delta L/L$ behaviors, one can get information on how the spin configurations along each orthogonal direction statistically change across the phase transitions, e.g., for $H \parallel a$, $(\Delta L/L)_c$ exhibits a jump at H_ζ but no detectable anomalies at H_η unlike $(\Delta L/L)_a$ and $(\Delta L/L)_b$ [Fig. 4(h)], signaling that at H_η the magnetic structure changes only within the ab plane. Interestingly, a remanence is seen for all the measured $\Delta L/L$'s, and the contraction along the a and b axes and the elongation along the c axis continue down to ~ -1 T upon reversal of a magnetic field, which is a hallmark of linear magnetostriction [41,42]. This would be attributed to the presence of remnant FIM components at 0 T. Indeed, the imperfection of the hysteresis-loop closing is also observed for the M-H curves at 4.2 K [Figs. 4(a) and 4(e)] so that piezomagnetism (and the piezoelectric effect) might also be expected in this compound.

C. Phase transitions in pulsed magnetic fields up to 50 T

In order to obtain an overall picture of the magnetostructural transitions and the accompanied ME effects in CBCNO, we have extended the experimental investigation towards a higher magnetic-field-and-temperature (H-T) regime. Figures 5(a)–5(f) show the magnetic-field dependence of M, ΔP, and the longitudinal $\Delta L/L$ measured at 4.2 K in pulsed magnetic fields of up to 50 T for $H \parallel b$ and for $H \parallel a$. All of the M and ΔP jumps observed in static fields are perfectly reproduced in the pulsed-field measurements as seen in the dM/dH and dP/dH peaks [insets of Figs. 5(a), 5(d) 5(b), and 5(e), respectively]. For $H \parallel b$, the series of metamagnetic transitions terminate at around 10 T, where ΔP reaches ~ 11 mC/m². Then, M monotonically increases between 10 and 50 T with almost no change in ΔP. $(\Delta L/L)_b$ also rapidly increases above 4 T where the transitions are much broadened presumably due to the stress caused by the glue as mentioned in Sec. III B, making the hysteresis larger than that in the M-H and ΔP-H curves [Fig. 5(c)]. For $H \parallel a$, on the other hand, another M step is observed at $\mu_0 H_\theta \approx 17$ T as indicated by the dashed line in Fig. 5(d). This M step is accompanied by a further increase in ΔP by ~ 3.5 mC/m², ultimately leading to almost the same magnitude of ΔP with that observed for $H \parallel b$. As shown in Fig. 5(f), $(\Delta L/L)_a$ also rapidly increases across this transition (the critical field is shifted to higher), indicating that the exchange striction is responsible for the further increase in ΔP as well. We conclude that the identical FIM state is realized above 20 T for $H \parallel b$ and $H \parallel a$, whereas the stabilization of an IM-FIM phase in a wide field range between 5 and 15 T is the characteristic feature for $H \parallel a$.

Figures 5(g)–5(j) show the temperature evolution of the M-H and ΔP-H curves for $H \parallel b$ and $H \parallel a$. As the temperature is increased up to 40 K, each critical field shifts to a slightly lower field in the field-increasing process, and the hysteresis gets smaller for both field directions. Here, an increase in ΔP larger than 10 mC/m² is seen. The hysteresis is almost closed above 57 K, whereas metamagnetic transitions accompanied by a large electric polarization change of $\Delta P = 5 \sim 10$ mC/m² still take place up to 75 K. Recalling that CBCO exhibits a giant field-induced ΔP only in a narrow temperature range between 62 and 69 K [17–19] [Fig. 1(b)], the temperature range showing giant ΔP is widened by more than ten times in CBCNO.

Furthermore, a metamagnetic transition accompanied by large ΔP of ~ 12 mC/m² is also observed for $H \parallel c$ in CBCNO when applying a magnetic field higher than 20 T (Fig. S2 in the Supplemental Material [37]). The hysteretic behaviors in the M-H and ΔP-H curves and their temperature evolutions are similar to those for $H \parallel b$ and $H \parallel a$, suggesting an AFM-FIM transition also for $H \parallel c$.

D. Magnetic phase diagram of CaBaCo₃.₉Ni₀.₁O₇

From the high-field M and ΔP measurements, we construct the H-T phase diagrams of CBCNO with trigonally twined domains as shown in Fig. 6. Here, we complementarily plot phase boundaries from the temperature scans of ε' measured at various magnetic fields (Fig. S3 in the Supplemental Material [37]). For $H \parallel b$, three additional phases, P, Q,
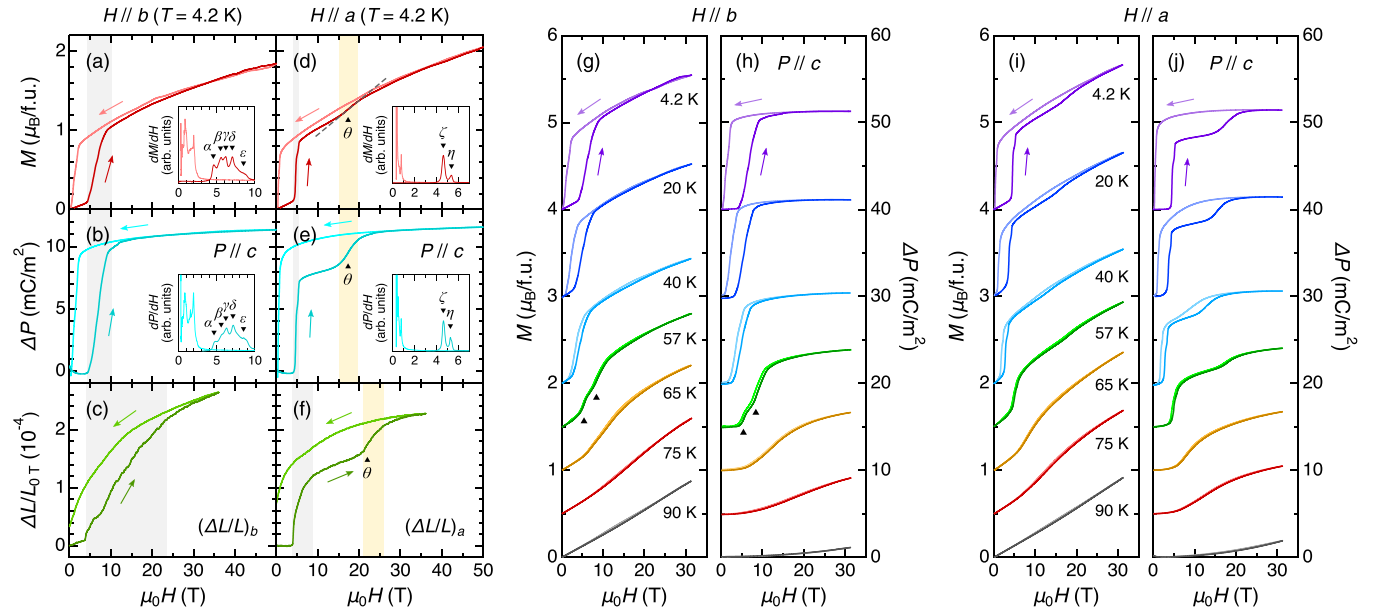
FIG. 5. [(a)–(f)] Magnetic-field dependence of [(a) and (d)] M, [(b) and (e)] ΔP along the c axis, and [(c) and (f)] $\Delta L/L$ along the field direction measured at 4.2 K in pulsed magnetic fields for $H \parallel b$ (sample No. 1) [(a)–(c)] and $H \parallel a$ (No. 2) [(d)–(f)]. The insets of (a), (b), (d), and (e) show the field derivative of each physical quantity in the low-field region. Here, the definitions of greek letters are identical with Fig. 4. Thanks to the simultaneous measurements of M and ΔP, the dM/dH and dP/dH anomalies are observed at exactly the same magnetic fields. [(g)–(j)] Magnetic-field dependence of [(g) and (i)] M and [(h) and (j)] ΔP along the c axis measured at selected temperatures for $H \parallel b$ (sample No. 1) [(g) and (h)] and $H \parallel a$ (No. 2) [(i) and (j)]. The data except for 90 K are vertically offset for clarity. Triangles in (g) and (h) denote the boundaries of phase Q [see Fig. 6(a)].

and R, which exist in a closed H-T regime, are identified around T_{N2} [Fig. 6(a)], e.g., the emergence of phase Q is clearly observed as a staircase shape in the M-H and ΔP-H curves at 57 K as indicated by triangles in Figs. 5(g) and 5(h). Such a complexity in the phase diagram compared to that of CBCO [Fig. 1(b)] should stem from the suppression of ferrimagnetism as well as the increase in the magnetic frustration caused by Ni doping, which would also be responsible for the broad multistage metamagnetic transitions observed at lower temperatures. For $H \parallel a$, on the contrary, the absence of a novel phase is confirmed, but instead the IM-FIM phase is found to be robust even near T_{N2}. Notably, the shape of the phase boundary between the IM-FIM and the FIM phases at H_θ is similar with that between the AFM and the IM-FIM phases at H_ζ, satisfying the relation $H_\theta \approx 4H_\zeta$ at all the measured temperatures below T_{N2}. This trend is reminiscent of the separation of identical phase transitions arising from the multidomain nature of the crystal as observed in GaV$_4$S$_8$ [43].

In order to understand the anisotropic nature of the H-T phase diagram for $H \parallel b$ and $H \parallel a$, we assume that: (i) the crystals contain three kinds of trigonally twinned domains (I, II, and III) with almost the same populations (see Fig. 7), (ii) each domain independently responds to an external magnetic field, and (iii) each domain does not undergo a spin-flop transition in the field region currently under consideration but undergoes an AFM-FIM transition at a critical field

$$H(\phi) = \frac{H_a H_b}{\sqrt{H_a^2 \cos^2 \phi + H_b^2 \sin^2 \phi}}, \quad (1)$$

when applying a magnetic field on the ab plane and at an angle of ϕ ($0 \leqslant \phi \leqslant \pi/2$) with b. Here, H_a and H_b are the critical fields for $\phi = 0$ and $\pi/2$, respectively. Under these assumptions, each domain should contribute to approximately one-third of the total electric polarization change of $\Delta P \approx 11$ mC/m^2. Bearing in mind that the critical fields in domains II and III are the same for $H \parallel b$ and $H \parallel a$, the observed M step with an increase in ΔP by ~ 3.5 mC/m^2 at a higher field H_θ can be attributed to the AFM-FIM transition in domain I [Figs. 5(d) and 5(e)]. This indicates that the magnetization easy axis is the a axis so that it would be reasonable to consider that the AFM spins are oriented along the b axis in zero field. Accordingly, for $H \parallel b$, the AFM-FIM transition in domain I should correspond to the onset of the series of metamagnetic transitions at H_α [Fig. 5(a)]. If we set $\mu_0 H_a = \mu_0 H_\theta = 17$ and $\mu_0 H_b = \mu_0 H_\alpha = 4$ T in Eq. (1), the critical fields in domains II/III for $H \parallel b$ and $H \parallel a$ can be estimated to $\mu_0 H(\pi/3) = 7.4$ and $\mu_0 H(\pi/6) = 4.6$ T, respectively. This qualitatively reproduces the main feature of the experimental results, showing significant changes in M and ΔP around 6 to 7 T for $H \parallel b$ and sharp metamagnetic transitions accompanied by $\Delta P \approx 7$ mC/m^2 around 4 to 5 T for $H \parallel a$ (Fig. 4). Figures 7(a) and 7(b) illustrate the ways of the AFM-FIM transitions in three kinds of domains for $H \parallel b$ and $H \parallel a$, respectively. Based on the above discussion, we draw the AFM-FIM phase boundaries for domain I (domains II/III) by gray solid (dashed) lines in Fig. 6.

The actual phase transitions in CBCNO seem more complicated. In real samples, the magnetic state of each domain would be affected by the local stress caused by magnetostriction in the surrounding domains. Indeed, for $H \parallel b$, dM/dH
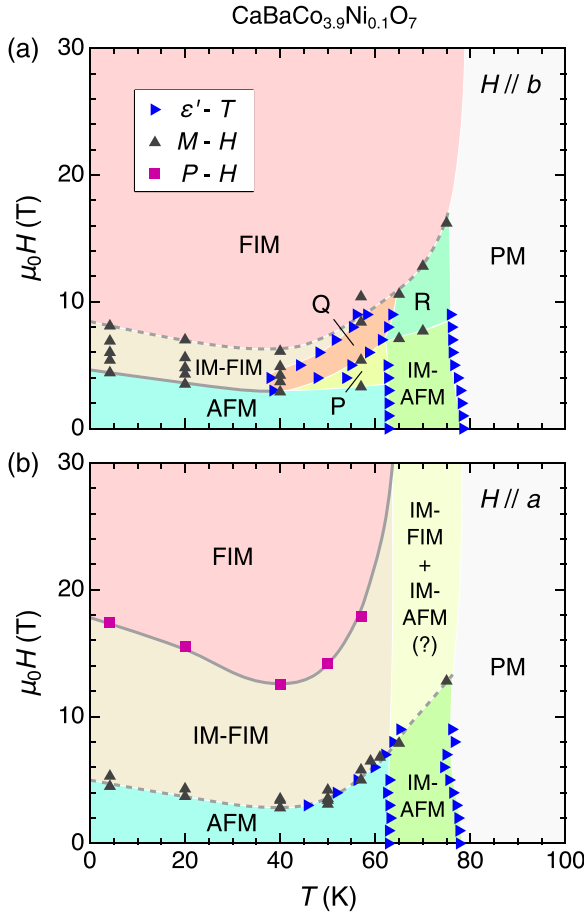
FIG. 6. H-T phase diagrams of as-grown CaBaCo$_{3.9}$Ni$_{0.1}$O$_7$ single crystals with trigonally twinned domains for (a) $H \parallel b$ (sample No. 1) and (b) $H \parallel a$ (No. 2). Phase boundaries are determined from the dielectric anomalies observed in the warming process at constant magnetic fields (Fig. S3 in the Supplemental Material [37]) and the dM/dH (or dP/dH) peaks observed in the field-increasing process in the pulsed-field measurements (Fig. 5). The possible AFM-FIM phase boundaries for domain I (domains II/III), defined as Fig. 7, are drawn by gray solid (dashed) lines.
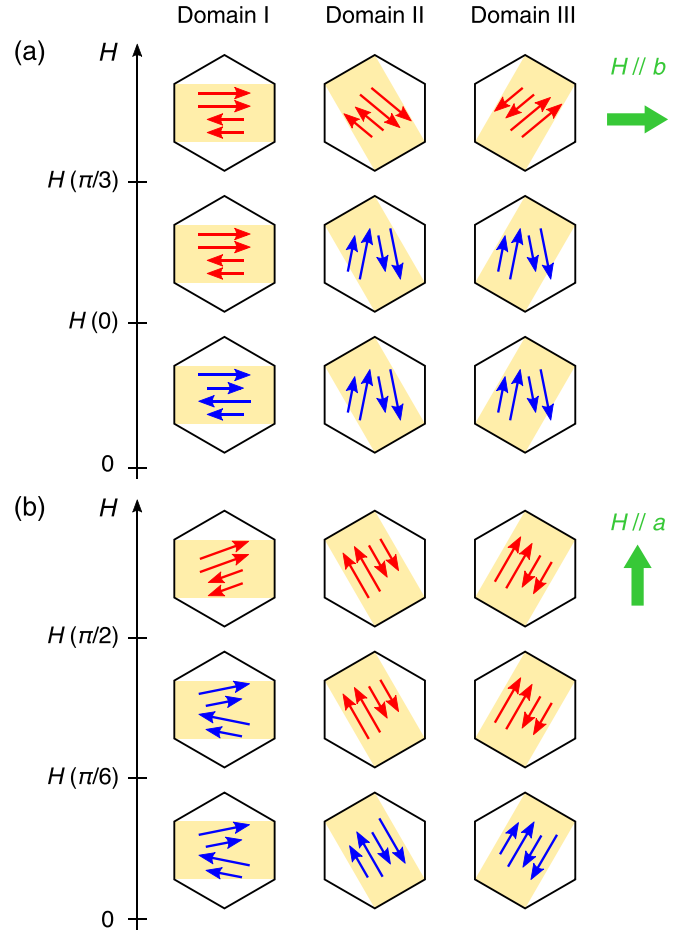

FIG. 7. Schematic of AFM-FIM transitions in three kinds of trigonally twinned domains for (a) $H \parallel b$ and (b) $H \parallel a$. The critical fields are defined by Eq. (1). Long (short) arrows represent the Co1/Co4 (Co2/Co3) spins. Spin configurations drawn by blue (red) correspond to the AFM (FIM) state. Although it is unclear how each spin is oriented relative to the magnetic field, a candidate magnetic structure is depicted for each domain assuming that the magnetization easy axis is the a axis, and a spin-flop transition does not occur in this field region.

and dP/dH exhibit broad humps with, at least, five peaks over $4 \sim 10$ T at low temperatures. Also for $H \parallel a$, the AFM-FIM transition in domains II/III is separated into two successive transitions at H_ζ and H_η. The importance of the stress on the magnetic state is corroborated by our magnetostriction measurements where the artificial shift of the critical fields seems to take place due to the glue covering the sample surface as mentioned in Secs. III B and III C. A further systematic investigation of the effects of pressure or stress on the magnetic phase diagram and the ME effect in CBCNO will be also meaningful.

IV. CONCLUSION

We have investigated the magnetic transitions and the ME effect of the polar magnet CaBaCo$_{3.9}$Ni$_{0.1}$O$_7$ up to 50 T using single crystals. At zero field, two AFM transitions are found with a second-order transition at $T_{N1} = 78$ K and a first-order transition at $T_{N2} = 62$ K both of which are accom-

panied by a dielectric anomaly and a negative change in ΔP of ~ -2 mC/m^2 along the c axis. On the application of a magnetic field along any crystallographic axes, a series of metamagnetic transitions with a giant positive change in ΔP of up to 11 to 12 mC/m^2 are observed in the whole temperature range below T_{N1}, demonstrating that the giant ME effect inherent in CBCO is enhanced. These transitions are accompanied by multistage expansion on the ab plane and contraction in the c axis of the crystal lattice, evidencing the emergence of a field-induced FIM state. Thus, we conclude that the enhancement of the giant ME effect is achieved by realizing the AFM ground state instead of the FIM one in low fields through Ni doping. The doping of nonmagnetic divalent cations, such as Zn^{2+} would also be a promising approach to enhance the ME effect of CBCO, which has not been investigated so far.

Ferrimagnets have recently attracted growing attention for their use in spintronics devices because of the

ferromagneticlike high controllability of the net magnetization and anti-ferromagnetic-like fast spin dynamics [44]. In this regard, the seeking for novel physical properties and functionalities in ferrimagnets gets more important, although there remain versatile research directions to them. Our present finding is an intriguing answer for them and potentially facilitates another discovery of the enhancement of the ME effect simply by chemical substitution in reported multiferroic materials.

[1] T. Kimura, T. Goto, H. Shintani, K. Ishizaka, T. Arima, and Y. Tokura, Magnetic control of ferroelectric polarization, Nature (London) **426**, 55 (2003).

[2] Y. Tokura, S. Seki, and N. Nagaosa, Multiferroics of spin origin, Rep. Prog. Phys. **77**, 076501 (2014).

[3] H. Katsura, N. Nagaosa, and A. V. Balatsky, Spin Current and Magnetoelectric Effect in Noncollinear Magnets, Phys. Rev. Lett. **95**, 057205 (2005).

[4] I. A. Sergienko and E. Dagotto, Role of the Dzyaloshinskii-Moriya interaction in multiferroic perovskites, Phys. Rev. B **73**, 094434 (2006).

[5] K. Taniguchi, N. Abe, T. Takenobu, Y. Iwasa, and T. Arima, Ferroelectric Polarization Flop in a Frustrated Magnet $MnWO_4$ Induced by a Magnetic Field, Phys. Rev. Lett. **97**, 097203 (2006).

[6] S. Park, Y. J. Choi, C. L. Zhang, and S.-W. Cheong, Ferroelectricity in an $S = 1/2$ Chain Cuprate, Phys. Rev. Lett. **98**, 057601 (2007).

[7] T. Arima, Ferroelectricity induced by proper-screw type magnetic order, J. Phys. Soc. Jpn. **76**, 073702 (2007).

[8] H. Murakawa, Y. Onose, S. Miyahara, N. Furukawa, and Y. Tokura, Ferroelectricity Induced by Spin-Dependent Metal-Ligand Hybridization in $Ba_2CoGe_2O_7$, Phys. Rev. Lett. **105**, 137202 (2010).

[9] I. A. Sergienko, C. Sen, and E. Dagotto, Ferroelectricity in the Magnetic E-Phase of Orthorhombic Perovskites, Phys. Rev. Lett. **97**, 227204 (2006).

[10] Y. J. Choi, H. T. Yi, S. Lee, Q. Huang, V. Kiryukhin, and S.-W. Cheong, Ferroelectricity in an Ising Chain Magnet, Phys. Rev. Lett. **100**, 047601 (2008).

[11] Y. Tokunaga, N. Furukawa, H. Sakai, Y. Taguchi, T. Arima, and Y. Tokura, Composite domain walls in a multiferroic perovskite ferrite, Nature Mater. **8**, 558 (2009).

[12] T. Arima, Spin-driven ferroelectricity and magneto-electric effects in frustrated magnetic systems, J. Phys. Soc. Jpn. **80**, 052001 (2011).

[13] V. Caignaert, V. Pralong, A. Maignan, and B. Raveau, Orthorhombic kagome cobaltite $CaBaCo_4O_7$: A new ferrimagnet with a T_C of 70 K, Solid State Commun. **149**, 453 (2009).

[14] V. Caignaert, V. Pralong, V. Hardy, C. Ritter, and B. Raveau, Magnetic structure of $CaBaCo_4O_7$: Lifting of geometrical frustration towards ferrimagnetism, Phys. Rev. B **81**, 094417 (2010).

[15] Z. Qu, L. Ling, L. Zhang, L. Pi, and Y. Zhang, Magnetic properties of the ferrimagnetic cobaltite $CaBaCo_4O_7$, Solid State Commun. **151**, 917 (2011).

[16] H. Iwamoto, M. Ehara, M. Akaki, and H. Kuwahara, Magnetoelectric property in $3d$ transition metal oxide with tetrahedral structure, J. Phys.: Conf. Ser. **400**, 032031 (2012).

[17] V. Caignaert, A. Maignan, K. Singh, C. Simon, V. Pralong, B. Raveau, J. F. Mitchell, H. Zheng, A. Huq, and L. C. Chapon, Gigantic magnetic-field-induced polarization and magnetoelectric coupling in a ferrimagnetic oxide $CaBaCo_4O_7$, Phys. Rev. B **88**, 174403 (2013).

[18] Y.-S. Chai, J.-Z. Cong, J.-C. He, D. Su, X.-X. Ding, J. Singleton, V. Zapf, and Y. Sun, Giant magnetostriction and non-saturating electric polarization up to 60 T in the polar magnet $CaBaCo_4O_7$, Phys. Rev. B **103**, 174433 (2021).

[19] T. Omi, Y. Watanabe, N. Abe, H. Sagayama, A. Nakao, K. Munakata, Y. Tokunaga, and T. Arima, Antiferromagnetic-to-ferrimagnetic phase transition with large electric-polarization change in a frustrated polar magnet $CaBaCo_4O_7$, Phys. Rev. B **103**, 184412 (2021).

[20] T. Omi, Doctoral Thesis submitted to the University of Tokyo, 2021.

[21] R. D. Johnson, K. Cao, F. Giustino, and P. G. Radaelli, $CaBaCo_4O_7$: A ferrimagnetic pyroelectric, Phys. Rev. B **90**, 045129 (2014).

[22] R. S. Fishman, S. Bordács, V. Kocsis, I. Kézsmárki, J. Viirok, U. Nagel, T. Rõõm, A. Puri, U. Zeitler, Y. Tokunaga, Y. Taguchi, and Y. Tokura, Competing exchange interactions in multiferroic and ferrimagnetic $CaBaCo_4O_7$, Phys. Rev. B **95**, 024423 (2017).

[23] K. Singh, V. Caignaert, L. C. Chapon, V. Pralong, B. Raveau, and A. Maignan, Spin-assisted ferroelectricity in ferrimagnetic $CaBaCo_4O_7$, Phys. Rev. B **86**, 024410 (2012).

[24] S. Bordács, V. Kocsis, Y. Tokunaga, U. Nagel, T. Rõõm, Y. Takahashi, Y. Taguchi, and Y. Tokura, Unidirectional terahertz light absorption in the pyroelectric ferrimagnet $CaBaCo_4O_7$, Phys. Rev. B **92**, 214441 (2015).

[25] M. M. Seikh, T. Sarkar, V. Pralong, V. Caignaert, and B. Raveau, Dramatic effect of A-site substitution upon the structure and magnetism of the "114" $CaBaCo_4O_7$ cobaltite, Phys. Rev. B **86**, 184403 (2012).

[26] M. M. Seikh, V. Pralong, V. Caignaert, and B. Raveau, Local melting of charge ordering in $CaBaCo_4O_7$ by Sr-doping, Z. Anorg. Allg. Chem. **640**, 1141 (2014).

[27] G. Aurelio, J. Curiale, F. Bardelli, R. J. Prado, L. Hennet, G. Cuello, J. Campo, and D. Thiaudière, Substitution site and effects on magnetism in Sr-for-Ca substituted $CaBaCo_4O_7$, J. Appl. Phys. **118**, 134101 (2015).

[28] J. Lohr, A. L. Larralde, J. Curiale, R. Sánchez, J. Campo, G. J. Cuello, D. Sheptyakov, L. Keller, M. Kenzelmann, and G. Aurelio, Intermediate magnetic phase of the magnetoelectric compound (Ca, Sr)$BaCo_4O_7$ described with the superspace formalism, Phys. Rev. B **102**, 134406 (2020).

[29] T. Sarkar, M. M. Seikh, V. Pralong, V. Caignaert, and B. Raveau, Magnetism of the "114" orthorhombic charge ordered $CaBaCo_4O_7$ doped with Zn or Ga: a spectacular valency effect, J. Mater. Chem. **22**, 18043 (2012).

[30] Y. Zou, Z. Qu, L. Zhang, W. Ning, L. Ling, L. Pi, and Y. Zhang, The effect of Al doping on the structure and magnetism in cobaltite $CaBaCo_4O_7$, J. Alloys Compd. **576**, 1 (2013).

[31] M. M. Seikh, A. K. Kundu, V. Caignaert, and B. Raveau, Gigantic effect of iron doping upon magnetism in the $\langle\langle 114\rangle\rangle$ magnetoelectric $CaBaCo_4O_7$, J. Alloys Compd. **656**, 166 (2016).

[32] T. Sarkar, M. M. Seikh, V. Pralong, V. Caignaert, and B. Raveau, Spectacular switching from ferrimagnetism to antiferromagnetism by zinc doping in "114" orthorhombic $CaBaCo_4O_7$, Appl. Phys. Lett. **100**, 232401 (2012).

[33] S. Yu, C. Dhanasekhar, V. Adyam, S. Deckoff-Jones, M. K. L. Man, J. Madéo, E. L. Wong, Takaaki Harada, M. B. M. Krishna, K. M. Dani, and D. Talbayev, Terahertz-frequency magnetoelectric effect in Ni-doped $CaBaCo_4O_7$, Phys. Rev. B **96**, 094421 (2017).

[34] C. Dhanasekhar, A. K. Das, R. Singh, A. Das, G. Giovannetti, D. Khomskii, and A. Venimadhav, Switching from pyroelectric to ferroelectric order in Ni-doped $CaBaCo_4O_7$, Phys. Rev. B **96**, 134413 (2017).

[35] H. Mitamura, S. Mitsuda, S. Kanetsuki, H. Aruga Katori, T. Sakakibara, and K. Kindo, Dielectric polarization measurements on the antiferromagnetic triangular lattice system $CuFeO_2$ in pulsed high magnetic fields, J. Phys. Soc. Jpn. **76**, 094709 (2007).

[36] A. Ikeda, Y. H. Matsuda, and H. Tsuda, Note: Optical filter method for high-resolution magnetostriction measurement using fiber Bragg grating under millisecond-pulsed high magnetic fields at cryogenic temperatures, Rev. Sci. Instrum. **89**, 096103 (2018).

[37] See Supplemental Material at http://link.aps.org/supplemental/10.1103/PhysRevB.105.214412 for additional experimental data.

[38] V. S. Zapf, V. F. Correa, P. Sengupta, C. D. Batista, M. Tsukamoto, N. Kawashima, P. Egan, C. Pantea, A. Migliori, J. B. Betts, M. Jaime, and A. Paduan-Filho, Direct measurement of spin correlations using magnetostriction, Phys. Rev. B **77**, 020404(R) (2008).

[39] A. Ikeda, S. Furukawa, O. Janson, Y. H. Matsuda, S. Takeyama, T. Yajima, Z. Hiroi, and H. Ishikawa, Magnetoelastic couplings in the deformed kagome quantum spin lattice of volborthite, Phys. Rev. B **99**, 140412(R) (2019).

[40] A. Miyata, H. Suwa, T. Nomura, L. Prodan, V. Felea, Y. Skourski, J. Deisenhofer, H.-A. Krug von Nidda, O. Portugall, S. Zherlitsyn, V. Tsurkan, J. Wosnitza, and A. Loidl, Spin-lattice coupling in a ferrimagnetic spinel: Exotic H-T phase diagram of $MnCr_2S_4$ up to 110 T, Phys. Rev. B **101**, 054432 (2020).

[41] A. S. Borovik-romanov, Piezomagnetism, linear magnetostriction and magnetooptic effect, Ferroelectrics **162**, 153 (1994).

[42] M. Jaime, A. Saul, M. Salamon, V. S. Zapf, N. Harrison, T. Durakiewicz, J. C. Lashley, D. A. Andersson, C. R. Stanek, J. L. Smith, and K. Gofryk, Piezomagnetism and magnetoelastic memory in uranium dioxide, Nat. Commun. **8**, 99 (2017).

[43] I. Kézsmárki, S. Bordács, P. Milde, E. Neuber, L. M. Eng, J. S. White, H. M. Rønnow, C. D. Dewhurst, M. Mochizuki, K. Yanai, H. Nakamura, D. Ehlers, V. Tsurkan, and A. Loidl, Néel-type skyrmion lattice with confined orientation in the polar magnetic semiconductor GaV_4S_8, Nature Mater. **14**, 1116 (2015).

[44] S. K. Kim, G. S. D. Beach, K.-J. Lee, T. Ono, T. Rasing, and H. Yang, Ferrimagnetic spintronics, Nature Mater. **21**, 24 (2022).